Optical scatterometry with relaxed model constraints

ANG JIANG,[1,†] **LINGJIE FAN,**[1,†] **JUNYI YE,**[1] **HAIWEI YIN,**[3]
MINJIA ZHENG,[1,7] **JIAJUN WANG,**[1,8] **MIN QIU,**[2]
AND LEI SHI[1,4,5,6,9]

[1]*State Key Laboratory of Surface Physics, Key Laboratory of Micro- and Nano-Photonic Structures (Ministry of Education) and Department of Physics, Fudan University, Shanghai 200433, China*
[2]*Zhejiang Key Laboratory of 3D Micro/Nano Fabrication and Characterization, School of Engineering, Westlake University, Hangzhou, Zhejiang 310030, China*
[3]*Shanghai Engineering Research Center of Optical Metrology for Nano-fabrication(SERCOM), Shanghai 200433, China*
[4]*Institute for Nanoelectronic devices and Quantum computing, Fudan University, Shanghai 200438, China*
[5]*Collaborative Innovation, Center of Advanced Microstructures, Nanjing University, Nanjing 210093, China*
[6]*Shanghai Research Center for Quantum Sciences, Shanghai 201315, China*
[7]*mjzheng@fudan.edu.cn*
[8]*jiajunwang@fudan.edu.cn*
[9]*lshi@fudan.edu.cn*
[†]*The authors contributed equally to this work*

Abstract: Optical scatterometry extracts structural and material properties of nanostructures from optical signal by solving the optical inverse problems (OIPs). It typically requires prior information for the establishment of structural models. Existing modeling methods are almost based on strict model constraints, which may oversimplify structural details. Here, we propose a strategy with relaxed model constraints. To deal with the expanded solution space caused by the relaxed constraints, the inverse design inspired optimization for optical scatterometry(IDO-OS) is developed by integrating automatic differentiation. We evaluated our method under both numerical simulation and experimental conditions. The results of numerical simulation demonstrate the performance of our method with an optimized spectral goodness-of-fit of 0.99 and a high degree of consistency with target structures. In the experiment, we integrate IDO-OS with hybrid metrology and thin plate splines algorithm to generate relaxed model constraints, and the reconstructed structures show excellent agreement with the measurements of transmission electron microscopy. This work establishes what we believe to be a new strategy for solving inverse problems in optical scatterometry, offering enhanced structural reconstruction capabilities while maintaining computational efficiency.

1. Introduction

Optical metrology [1–4] studies the interaction between light and the object under test to make measurements. It plays a crucial role across diverse fields due to its non-contact nature and high-speed capabilities. Optical scatterometry [5–8], also called optical critical dimension metrology, is a widely used optical metrology method for morphology reconstruction and material characterization of periodic micro and nano- structures. It includes two fundamental components: experimental measurement and optical inverse problems(OIPs) [9–12]. The experimental measurement involves the acquisition of optical signal using specialized instrumentation, and the OIPs focus on extracting structural and material properties from the measured signal. Solving OIPs is an important and difficult part in optical scatterometry, which is typically achieved

through a combination of simulations and algorithms [13–16]. For simulation, the model of the sample to be tested is constructed with numerical methods to calculate the corresponding optical signal; for algorithms, different strategies are employed to adjust model parameters to find the best model whose simulated optical signal matches the target signal.

When solving OIPs, it is usually necessary to combine prior information to establish the structure model to reduce the complexity [17–20]. For existing methods, strict model constraints are used when constructing models. So, the solution space is defined by the parameters of the specified models. For example, a trapezoidal model (Fig. 1(a)) typically involves five parameters, resulting in its solution space consisting of the same dimension. These strict model constraints simplify the number of parameters and improve computational efficiency, but lead to structures that are highly dependent on particular model constraints. Practical structures actually have more detailed shape features, requiring relaxed model constraints with more structural parameters. Since the relaxation of model constraints, the solution space will be significantly expanded and contain structures with different geometric profiles, as shown in Fig. 1(b). However, existing optimization methods have difficulty dealing with such an expanded solution space due to substantial computational resources. To introduce relaxed model constraints in optical scatterometry, new optimization methods are on demand.
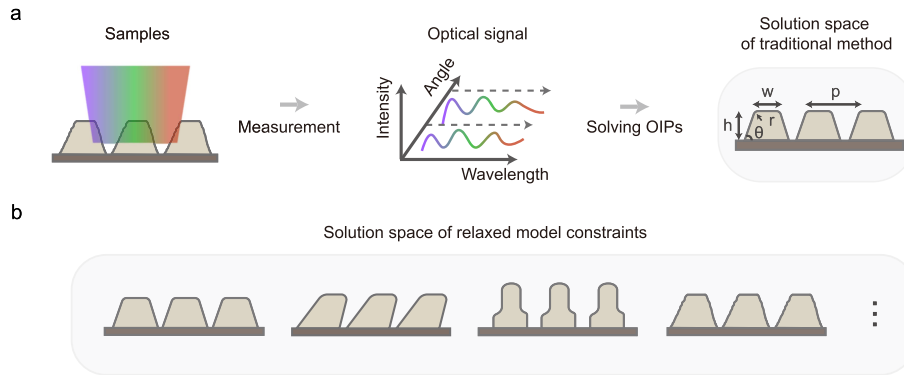
Fig. 1. Schematic diagram of the solution space of traditional methods and our method with relaxed model constraints. (a) When solving OIPs from the measured optical signal, traditional methods construct model with strict model constraints. For the trapezoidal model, the solution space can be a 5-dimesions space containing parameter w, p, h, θ and r. (b) The solution space of relaxed model constraints will be significantly expanded and contain structures with different geometric profiles.

In recent years, optical inverse design is developing rapidly in solving OIPs and many optimization methods have been developed [21,22]. In optical inverse design, the optimization of a large number of parameters has been extensively studied. Among these studies, the adjoint method [23] is proposed so that only two simulations are needed to obtain gradients of all parameters, which eventually makes gradient-based optimization of a large number of parameters practical. Additionally, the advent of automatic differentiation [24,25] has provided a new method for obtaining parameter gradients. These methods make it possible to optimize a large number of parameters with reasonable computing resources, but they are closely integrated with the optical inverse design itself and are usually used in topology optimization [26]. In optical scatterometry, it is only necessary to adjust the shape of the model. Therefore, directly applying methods from optical inverse design to optical scatterometry is not suitable.

To combine the advantages of these optimization methods into the applications of optical scatterometry, we develop an OIPs' solving approach by integrating automatic differentiation,

termed inverse design inspired optimization for optical scatterometry (IDO-OS). IDO-OS can compute gradients for all structural parameters after a single forward simulation and has a high degree of compatibility with optical scatterometry scenes. The principle of IDO-OS and the workflow of optical scatterometry with relaxed model constraints are introduced in the Methods section. In the Results and discussion section, we evaluate IDO-OS's performance in solving OIPs under the numerical simulation condition. The optimized spectrum achieves a goodness-of-fit (GOF) of 0.99, and the results are highly consistent with the target structure. In the experiment, we combine thin plate splines algorithm (TPS) [27] and hybrid metrology [28] to provide prior information for some inclined silicon-on-insulator (SOI) gratings. Then we transform the prior structural information into relaxed model constraints and solve the OIPs. The GOF of the spectrum reaches 0.98, and the reconstructed structures agree well with the transmission electron microscopy (TEM) measurements.

2. Methods

The fundamental principles of IDO-OS are shown in Fig. 2(a), comprising two essential components: forward and backward processes. The forward process employs rigorous coupled wave analysis (RCWA) [29] to calculate the optical signal from nanostructures. The RCWA simulation is a method for solving Maxwell's equations based on plane-wave expansion. It involves dividing the structure into differential layers, solving eigenvalue equations in each differential layer on the plane-wave basis, and constructing the transmission matrix between layers according to the boundary conditions. As expressed in Eq. (1) and Eq. (2):

$$\begin{pmatrix} c_i \\ d_i \end{pmatrix} = \begin{pmatrix} e^{j\phi_i} & 0 \\ 0 & e^{-j\phi_i} \end{pmatrix} \begin{pmatrix} a_i \\ b_i \end{pmatrix} \tag{1}$$

$$\begin{pmatrix} a_i \\ b_i \end{pmatrix} = T_i \begin{pmatrix} c_{i-1} \\ d_{i-1} \end{pmatrix} \tag{2}$$

the electric field of a specific plane wave in layer i can be represented as a superposition of forward and backward propagating components, with coefficients denoted as a_i and b_i, respectively. The propagation of an electromagnetic wave within the layer i introduces a phase shift ϕ_i, represented by a diagonal matrix containing phase propagation factors. At the interface between adjacent layers (i-1 and i), propagation of electromagnetic wave must satisfy boundary conditions, represented by transfer matrix T_i. So based on these equations, the electromagnetic field distribution in different differential layers can be calculated. The backward process is described by Eq. (3) and Eq. (4):

$$\begin{pmatrix} \partial r/a_i \\ \partial r/b_i \end{pmatrix} = \begin{pmatrix} e^{-j\phi_i} & 0 \\ 0 & e^{j\phi_i} \end{pmatrix} \begin{pmatrix} \partial r/c_i \\ \partial r/d_i \end{pmatrix} \tag{3}$$

$$\begin{pmatrix} \partial r/c_{i-1} \\ \partial r/d_{i-1} \end{pmatrix} = T_i^T \begin{pmatrix} \partial r/a_i \\ \partial r/b_i \end{pmatrix} \tag{4}$$

It involves obtaining all differential layer gradient matrices by automatic differentiation [23,24], r denotes the corresponding optical signal. Automatic differentiation is a technique widely used in machine learning to implement backpropagation in a neural network without a manually-computed derivative. The core idea behind automatic differentiation is to efficiently compute gradients by applying the chain rule to the computational graph of the function. The analytical construction

of the forward process by RCWA enables gradient computation for structural parameters through the chain rule, and by employing automatic differentiation, we can acquire the gradients for all parameters through a single forward simulation.

Based on IDO-OS, we introduce relaxed model constraints into optical scatterometry. Fig. 2(b) shows the comparative workflows between traditional approaches and this work, and the differences are highlighted with different colors. In this work, we allow the parameters of each differential layer to be optimized. The solution space includes the combined thickness, width, and center position of each differential layer. As long as the number of differential layers is sufficient, the parameters of all differential layers can be used to describe any shape. Then, optimizing the parameters of these differential layers under the prior imformation, we can obtain an optimization with higher degrees of freedom and more structural details than the specific geometric model constraints, namely relaxed model constraints.
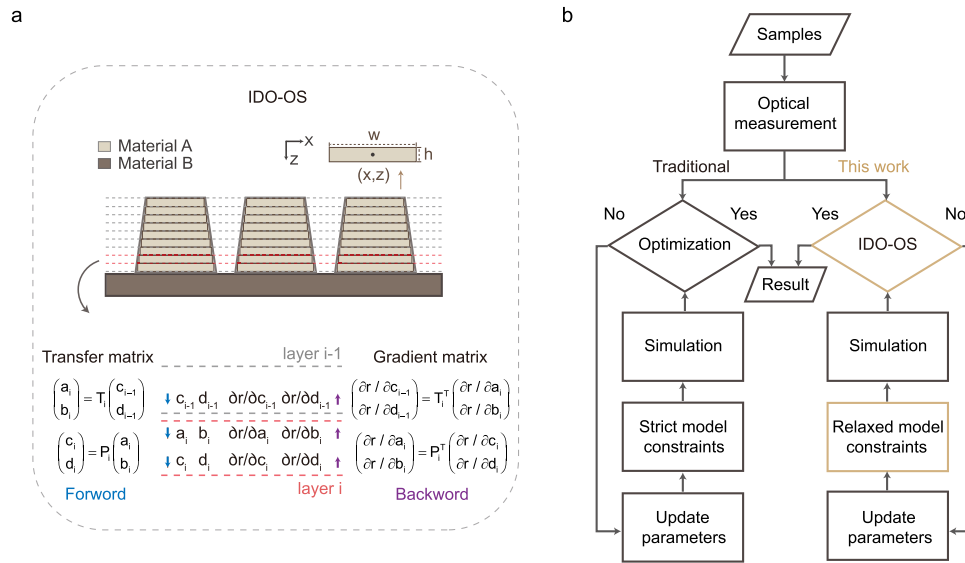
Fig. 2. The principle of IDO-OS and the workflow of optical scatterometry with relaxed model constraints. (a) Schematic diagram of IDO-OS. The upper section illustrates the forward modeling. The structure in a unit cell is described by rectangular differential layers with thickness h, width w, and center (x, z). The lower section shows the forward and backward processes of IDO-OS. Here, a_i, b_i and c_i, d_i are the forward and backward propagation coefficients of the electric field at the upper and lower interface in layer i, respectively. T_i represents the transfer matrix between layer i-1 and layer i. P_i denotes the propagation matrix in layer i. r denotes the corresponding optical signal. (b) The workflow of optical scatterometry with strict model constraints and relaxed model constraints.

Figure 3 illustrates the time required for obtaining all gradients once under relaxed model constraints by the traditional method and IDO-OS. Here, we only calculate one spectral point in the RCWA. The computations are performed on a 12th Gen Intel Core i7-12700F processor with 16 GB memory. Traditional optimization methods, relying on numerical differentiation, require multiple forward processes (indicated by the blue arrow in Fig. 2(a)) to compute gradients of all parameters. The computational time for these methods can be simply expressed as $n * ft$, where n denotes the parameter count and ft represents the forward process time. IDO-OS, intergrating automatic differentiation, executes a single forward process followed by gradient computation in the backward process. Its computational time is simply expressed as $ft + n * bt$, where bt represents the backward process time. Under relaxed model constraints, which typically involve numerous

differential layers, the forward process time substantially exceeds the backward process time. This fundamental difference explains the significant computational advantage of IDO-OS over traditional methods. The memory overhead introduced by automatic differentiation is negligible, consuming merely 0.3% of total memory resources.
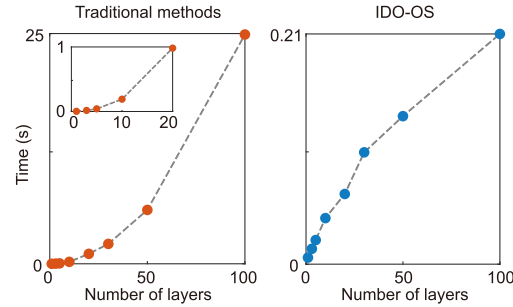

Fig. 3. Time required for obtaining all gradients once under relaxed model constraints of one spectral point by the traditional method and IDO-OS. The thick dots represent the sampling points. The graph in the upper left corner shows details within the vertical coordinate range of 0 to 1 s and the horizontal coordinate range of 0 to 20.

3. Results and discussion

3.1. Numerical simulation condition

We first evaluate the performance of the IDO-OS optimization method under the numerical simulation condition. We use the simulated constructed sample as the target sample and optimize with relaxed model constraints to verify the performance. We set the one-dimensional SOI grating as the target structure. We also set the structure as a slanted grating and add radian at the top to increase structure complexity, as shown in the first picture in Fig. 4(a). The material of the substrate and the top layer are set as monocrystalline silicon and amorphous silicon, respectively, and the middle layer material is set as silicon dioxide.
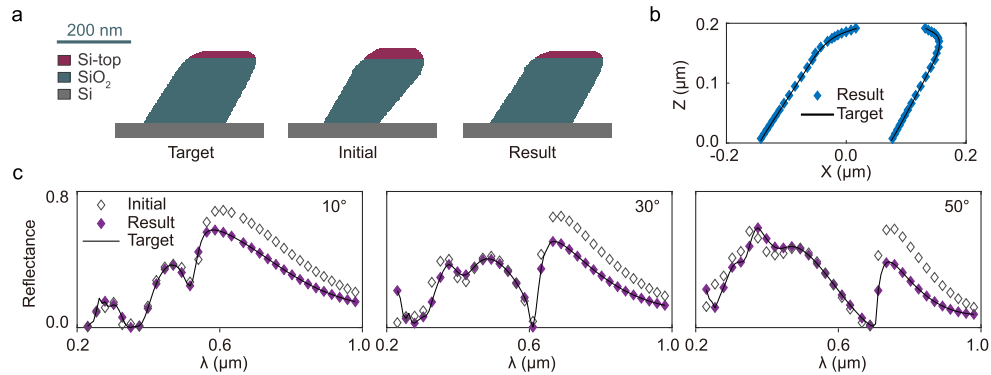
Fig. 4. Results in numerical simulation condition. (a) Schematic of the structures in a unit cell. (b) Comparison between the result structure and the target structure. (c) Specular reflectance spectra of the initial structure, the result structure and the target structure at incident angles of 10°, 30° and 50°.

When establishing models with the prior information, we transform the prior information into relaxed model constraints. The target structure is divided into many differential layers, and the

positions of the differential layers are used to describe the shape. During optimization, we keep the difference between the position of the layers in the model structure and the target structure below a set threshold as constraints. In the traditional method, the upper curve is often described by a circular arc or a Bessel curve. For the circular arc, it simplifies the details of the curve; for the Bezier curve, the number of parameters will become large when choosing a high-order Bezier curve or involving many curves in structure, and it cannot be ensured that the optimized structure retains the features of the prior information. In contrast, we combine relaxed model constraints to ensure that the optimized structure can retain more information about the prior structure information.

The setup is as follows: we establish the model with 70 differential layers. The number of layers represents a hyperparameter in RCWA modeling, which can be selected based on spectral convergence. The material of the substrate is set as monocrystalline silicon. The material of the top 20 layers and the last 50 layers is set as amorphous silicon and silicon dioxide, respectively. For the top 30 layers, we set the difference threshold of the relative positions of the model structure and the target structure to 1 nm. We choose such a threshold to correspond to the experimental condition in Section 3.2, which explained in detail in Section 3.2. For the latter 40 layers, the positions of both sides of the differential layer are fitted linearly after each optimization and ensure the edge of the differential layer falling on the fitted line. The linear fitting constraint is specifically motivated by the characteristics of the target area, which exhibits a flat profile without obvious detailed structure in the prior information. The initial structure of the model is shown in the second picture in Fig. 4(a). The period and material of the model are set as the same as the target model. The optimization uses the Adam optimizer [30] with a learning rate of 1e-5. We choose mean squared error as the loss function.

$$\chi^2 = \sum_{k=1}^{N} \omega_k [e_k - s_k(x)]^2 \tag{5}$$

In Eq.(5), ω denotes the weight coefficient, e denotes the experimental signal, s denotes the simulation signal and k denotes the sampling number. ω_k is defined by the equation $\omega_k = 1/\sigma^2(e_k)$, where σ indicates the standard deviation of experimental signal [18]. In the numerical simulation condition, since the target spectrum is simulated and there are no errors, we set ω_k to the constant value of 1. The target signal is set as s-polarized specular reflectance spectra across a 200-1000 nm wavelength range at incident angles of 10°, 30° and 50°.

The optimized structure is shown in the third picture in Fig. 4(a), and the result is highly consistent with the target structure as shown in Fig. 4(b) (for clarity, the number of the points in Fig. 4(b) is less than the number of differential layers). Fig. 4(c) shows the simulated spectra of the initial structure, the result structure, and the target structure. The initial spectrum exhibited a GOF score of 0.90, and the optimized spectrum achieved a GOF score of 0.99. So in the numerical simulation condition, our method shows excellent performance. The optimized structure and the target structure are almost identical by using relaxed model constraints.

3.2. Experiment condition

In the experiment, the prior structure information usually comes from two sources, one from the pre-set structure in the process, and the other from the results of other metrology tools. The pre-set structure is not always consistent with the practical structure, so we obtain prior structure information from other metrology tools, which can also be called hybrid metrology [28]. By definition, hybrid metrology involves the combination of two or more metrology tools to analyze the same sample. It emerges as a powerful strategy to overcome the inherent limitations of individual measurement techniques. We combined hybrid metrology to provide relaxed model constraints. It is worth mentioning that hybrid metrology not only provides initial structural

information but also acts as a regularization mechanism, effectively preventing convergence to physically unrealistic local extrema. The sample is first measured by TEM. The edge detection algorithm [31] is then applied to the TEM image to extract the shape. However, if every sample is measured with TEM, the cost and time will increase a lot. Considering that a batch of samples is often processed using the same manufacturing process at the same time, these samples are often very similar in the treatment of the manufacturing process. So, we propose a strategy to obtain prior structure information on the same class of samples from the same manufacturing process. We perform TEM on only one sample and use TPS [26] to estimate the structure of other samples without TEM. Fig. 5 shows a schematic of this strategy. The core idea of this method is to describe the manufacturing process as the mapping of the nominal structure and TEM structure of one sample and then applying the mapping to other samples. Firstly, the edge detection algorithm is used to obtain the shape of the sample measured by TEM. Secondly, the extracted shape is processed into a model structure suitable for RCWA modeling. Thirdly, mapping the relationship from the nominal structure to the TEM structure with TPS. Finally, the estimated TEM structures of the others can be calculated using the mapping relationship and other nominal structures. We emphasize that the TEM test is not necessary. Alternative metrology techniques, such as scanning electron microscopy or atomic force microscopy, can equally serve as sources of prior information.
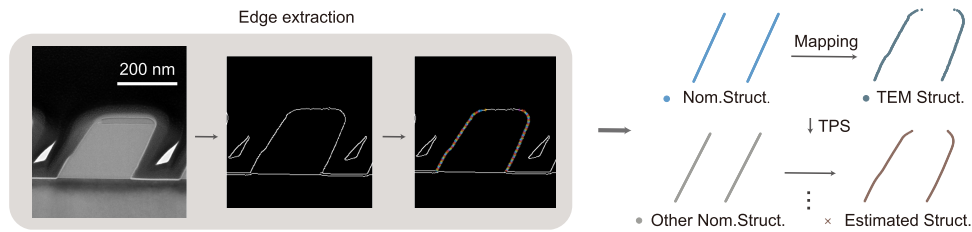

Fig. 5. Schematic diagram of Edge extraction and TPS algorithm for providing prior information of the batch of samples.

We process two inclined SOI gratings. The material of the substrate and the top layer are set as monocrystalline silicon and amorphous silicon, respectively, and the middle layer material is set as silicon dioxide. The nominal period is 400 and 450 nm. Since the period can be clearly described by the diffraction equation, it is obtained by solving the diffraction equation.

$$\sin\theta_i + \sin\theta_m = m\frac{\lambda}{\Lambda} \tag{6}$$

In Eq.(6), i denotes the incident light, m denotes the diffraction order, λ denotes the wavelength of the light and Λ denotes the period of the sample. We choose angular-resolution spectroscopy to measure optical signal. The experimental setup is shown in Fig. 6. The experimental procedure consists of two steps. The first step is to measure the unpatterned area of the sample to obtain the material information and the second step is to measure the structure region of the sample. For the first step, we measure the specular reflectance spectra polarized with s at incident angles of 10°, 30° and 50°. We then construct a thin film model and use the Cauchy equations and the Tauc-Lorentz dispersion equation [32] for the silicon dioxide layer and the amorphous silicon layer, respectively. We choose the Levenberg-Marquardt algorithm [33] to optimize material parameters. In the second step, we perform measurements on the structure region with the same optical configuration. The prior structure information is obtained by TEM on the sample whose nominal period is 400 nm. We establish the model with 100 differential layers. The material of the substrate is set as monocrystalline silicon. The material of the top 12 layers and the last 88 layers is set as amorphous silicon and silicon dioxide, respectively. We used the predicted

structure obtained by the TPS algorithm shown in Fig. 5 to perform differential layer initialization. The process begins by assigning uniform thickness values to all differential layers. Subsequently, we derive vertex coordinates for each differential layer through interpolation of the prior contours at different thickness positions. The width and center point of each differential layer are then calculated based on these vertex coordinates. Considering that there is a small stepped structure on the left contour of the TEM, we apply threshold constraints in the top and step areas, and linear fitting in other areas. The prior information is transformed into relaxed model constraints, and the difference threshold is set to 1 nm. We choose such a threshold to combine the advantages of the two metrology tools in hybrid metrology. The area with threshold constraints has rich and detailed features. Given that the wavelength of light used in optical scatterometry typically greatly exceeds the electron wavelength, TEM demonstrates superior capability in detecting these features compared to optical scatterometry. The threshold constraint thus serves to appropriately limit the scope of optical scatterometry. As a hyperparameter, the threshold value influences the model's regularization intensity, with lower thresholds corresponding to stronger regularization effects. Then, as we did in the numerical simulation condition, the optimization used the Adam optimizer with a learning rate of 1e-5. We choose mean squared error as the loss function and the target signal is set as s-polarized specular reflectance spectra across a 200-1000 nm wavelength range at incident angles of 10°, 30° and 50°.
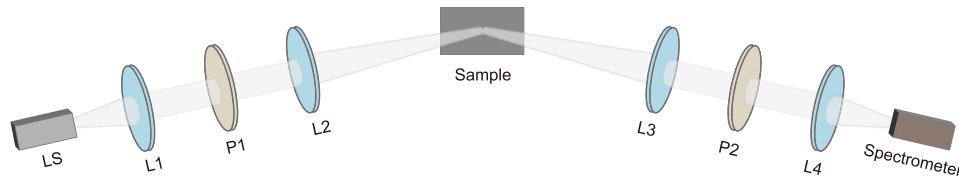
Fig. 6. Schematic view of the experimental setup consisting of lens (L), polarizers(P), light source (LS) and spectrometer.

According to the diffraction equation, the periods of the two samples are 400.01 nm and 449.05 nm, respectively. Fig. 7(a) shows the optimized structures. We also test another sample by TEM and compare the TEM structure with the measured structure. It can be found that the measured results agree well with the TEM structures. Fig. 7(b) shows the optimized spectra of the two samples. The GOF of the optimized spectral of the two samples reaches 0.980 and 0.977, indicating that the spectra of the optimized structures are highly consistent with the experimental spectra. To quantitatively validate our method's accuracy, we performed a comparative analysis between TEM and IDO-OS measurements for Sam2. The critical dimension parameters illustrated in Fig. 8 are extracted by repeated sampling and statistical averaging. As shown in Table 1, the largest absolute deviation is 2.9 nm, indicating high accuracy of our method.

Table 1. Measured parameters of TEM and IDO-OS for Sam2, and the absolute deviation

| Parameters	TEM	IDO-OS	Absolute deviation
h1 (nm)	22.6	21.4	1.2
h2 (nm)	186.9	188.8	1.9
w (nm)	251.2	248.3	2.9
a1 (∘)	58.7	59.2	0.5
a2 (∘)	115.7	115.9	0.2

4. Conclusion

In summary, we propose a method with relaxed model constraints in optical scatterometry. Compared with traditional methods, which are based on strict geometric model constraints, our method has higher degrees of freedom and can reflect more structural details. Tests in both numerical simulation and experimental conditions show that our method has excellent performance. Our method provides a new strategy for solving inverse problems in optical scatterometry and we also propose a strategy for achieving accurate, low-cost measurements for batch samples in manufacturing processing.
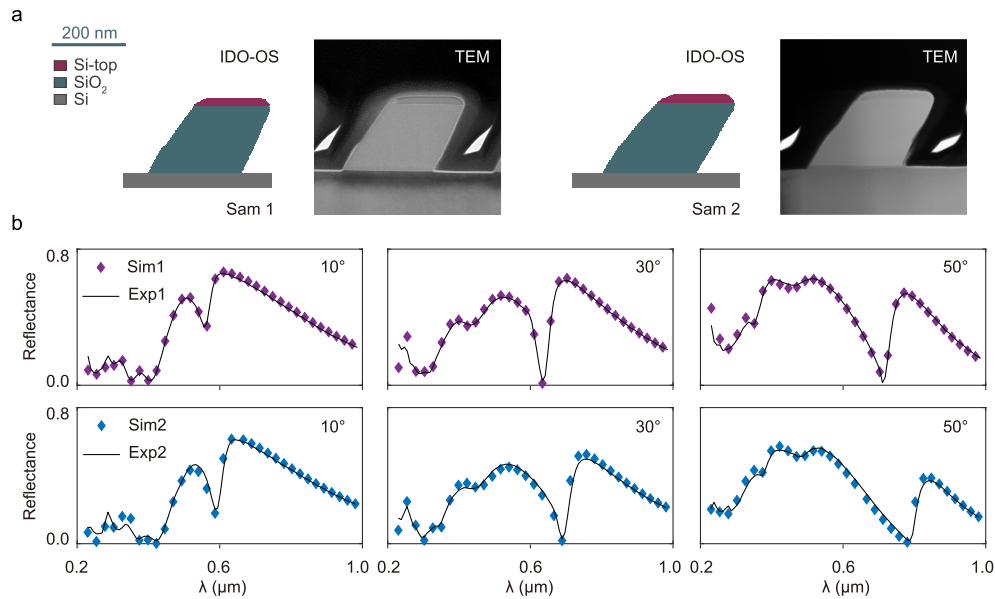
Fig. 7. Results in experimental condition. (a) Comparison between IDO-OS results and TEM results in a unit cell. (b) Simulated specular reflectance spectra and the experimental spectra of sam1, sam2 at incident angles of 10°, 30° and 50°.
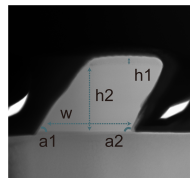
Fig. 8. The critical dimension parameters we extracted in TEM result.

Disclosures. H.Y. have financial interest in Ideaoptics Instruments Co., Ltd. The remaining authors declare no competing interests.

Data availability. The data that support the findings of this study are available on request from the corresponding author upon reasonable request.

References

1. N. G. Orji, M. Badaroglu, B. M. Barnes, *et al.*, "Metrology for the next generation of semiconductor devices," Nat. Electron. **1**(10), 532–547 (2018).
2. P. J. De Groot, "A review of selected topics in interferometric optical metrology," Rep. Prog. Phys. **82**(5), 056101 (2019).
3. C. Zuo, J. Qian, S. Feng, *et al.*, "Deep learning in optical metrology: a review," Light:Sci. Appl. **11**(1), 1–54 (2022).
4. M. Tanksalvala, C. L. Porter, Y. Esashi, *et al.*, "Nondestructive, high-resolution, chemically specific 3d nanostructure characterization using phase-sensitive euv imaging reflectometry," Sci. Adv. **7**(5), eabd9667 (2021).
5. A. C. Diebold, A. Antonelli, and N. Keller, "Perspective: Optical measurement of feature dimensions and shapes by scatterometry," APL Mater. **6**(5), 058201 (2018).
6. K. Meng, B. Jiang, and K. Youcef-Toumi, "Neural network assisted multi-parameter global sensitivity analysis for nanostructure scatterometry," Appl. Surf. Sci. **570**, 151219 (2021).
7. Z.-Y. Fu, W.-H. Chein, F.-S. Yang, *et al.*, "Artificial-neural-network-assisted duv scatterometry for ocd on har sub-micron structures," in *Metrology, Inspection, and Process Control XXXVII*, (2023), pp.79–89.
8. P. Zhang, F. Peng, D. Yang, *et al.*, "A laplace sensitivity operator enhances the calculation efficiency of ocd metrology," Opt. Express **31**(2), 2147–2160 (2023).
9. T. Li, A. Chen, L. Fan, *et al.*, "Photonic-dispersion neural networks for inverse scattering problems," Light:Sci. Appl. **10**(1), 154 (2021).
10. C. Guo, J. Liu, H. Gu, *et al.*, "Ensemble learning-fused solution to the inverse problem in integrated optical critical dimension metrology," IEEE Trans. Instrum. Meas. **74**, 1–15 (2025).
11. S. Liu, X. Chen, T. Yang, *et al.*, "Machine learning aided solution to the inverse problem in optical scatterometry," Measurement **191**, 110811 (2022).
12. L. Fan, A. Chen, T. Li, *et al.*, "Thin-film neural networks for optical inverse problem," Light: Advanced Manufacturing **2**(4), 1–402 (2021).
13. V. Ferreras Paz, S. Peterhänsel, K. Frenner, *et al.*, "Solving the inverse grating problem by white light interference fourier scatterometry," Light:Sci. Appl. **1**(11), e36 (2012).
14. X. Chen, S. Liu, C. Zhang, *et al.*, "Improved measurement accuracy in optical scatterometry using correction-based library search," Appl. Opt. **52**(27), 6726–6734 (2013).
15. C. Guo, Y. Shi, H. Wu, *et al.*, "A combination of library search and levenberg-marquardt algorithm in optical scatterometry," Thin Solid Films **767**, 139670 (2023).
16. M. Godi Tchéré, S. Robert, J. Dutems, *et al.*, "Characterization of a perfect sinusoidal grating profile using an artificial neural network for plasmonic-based sensors," Appl. Opt. **63**(14), 3876–3884 (2024).
17. M. L. Gödecke, K. Frenner, and W. Osten, "Model-based characterisation of complex periodic nanostructures by white-light mueller-matrix fourier scatterometry," Light: Advanced Manufacturing **2**(2), 1–250 (2021).
18. S. Liu, X. Chen, and C. Zhang, "Development of a broadband mueller matrix ellipsometer as a powerful tool for nanostructure metrology," Thin Solid Films **584**, 176–185 (2015).
19. D. Yang, W. Liang, S. Wang, *et al.*, "Enhanced inverse problem solution in angle-resolved scatterometry using a combination of library search and particle swarm algorithm," Opt. Laser Technol. **184**, 112424 (2025).
20. W.-H. Chein, F.-S. Yang, Z.-Y. Fu, *et al.*, "Non-integral model-based scatterometry for single-structure ocd metrology," in *Modeling Aspects in Optical Metrology IX*, vol. 12619 (SPIE, 2023), pp.137–145.
21. S. Molesky, Z. Lin, A. Y. Piggott, *et al.*, "Inverse design in nanophotonics," Nat. Photonics **12**(11), 659–670 (2018).
22. W. Ma, Z. Liu, Z. A. Kudyshev, *et al.*, "Deep learning for the design of photonic structures," Nat. Photonics **15**(2), 77–90 (2021).
23. T. W. Hughes, M. Minkov, I. A. Williamson, *et al.*, "Adjoint method and inverse design for nonlinear nanophotonic devices," ACS Photonics **5**(12), 4781–4787 (2018).
24. A. G. Baydin, B. A. Pearlmutter, A. A. Radul, *et al.*, "Automatic differentiation in machine learning: a survey," Journal of machine learning research **18**, 1–43 (2018).
25. M. Minkov, I. A. Williamson, L. C. Andreani, *et al.*, "Inverse design of photonic crystals through automatic differentiation," ACS Photonics **7**(7), 1729–1741 (2020).
26. A. Takezawa and M. Kobashi, "Design methodology for porous composites with tunable thermal expansion produced by multi-material topology optimization and additive manufacturing," Composites, Part B **131**, 21–29 (2017).
27. J. Zhao and H. Zhang, "Thin-plate spline motion model for image animation," in *Proceedings of the IEEE/CVF Conference on Computer Vision and Pattern Recognition*, (2022), pp.3657–3666.
28. L. Crouzier, A. Delvallée, S. Ducourtieux, *et al.*, "Development of a new hybrid approach combining afm and sem for the nanoparticle dimensional metrology," Beilstein J. Nanotechnol. **10**, 1523–1536 (2019).
29. M. Moharam, E. B. Grann, D. A. Pommet, *et al.*, "Formulation for stable and efficient implementation of the rigorous coupled-wave analysis of binary gratings," J. Opt. Soc. Am. A **12**(5), 1068–1076 (1995).
30. D. P. Kingma and J. Ba, "Adam: A method for stochastic optimization," in *3rd International Conference on Learning Representations, ICLR*, (2015).
31. J. Jing, S. Liu, G. Wang, *et al.*, "Recent advances on image edge detection: A comprehensive review," Neurocomputing **503**, 259–271 (2022).
32. H. Chen and W. Shen, "Perspectives in the characteristics and applications of tauc-lorentz dielectric function model," Eur. Phys. J. B **43**(4), 503–507 (2005).
33. H. P. Gavin, "The levenberg-marquardt algorithm for nonlinear least squares curve-fitting problems," Department of Civil and Environmental Engineering Duke University August **3**, 1–23 (2019).